k_t. We denote by D_{ft} the (complex) Fourier coefficient of frequency f ($f = 1, \ldots, N_f$) for trace t, $t = 1, \ldots, N_t \leq N_r N_s$. Ideally, after they have been corrected for normal move-out (18), all traces corresponding to the same midpoint carry coherent information. If there were no need for statics corrections, all signals, stacked by their common midpoint, should be in phase and yield a maximum for the total power

$$E(\mathbf{S}, \mathbf{R})$$

$$= \sum_k \sum_f \left| \sum_t \exp[2\pi i\, f(S_{s_t} + R_{r_t})] D_{ft} \delta_{kk_t} \right|^2 \quad (7)$$

In Eq. 7, the statics corrections $\mathbf{S} = (S_1, \ldots, S_{N_s})$ and $\mathbf{R} = (R, \ldots, R_{N_r})$ are now considered independent variables. Their optimum values are found by maximizing the power E. Equation 7 highlights the multimodal nature of E, which, even for relatively low-dimensional $\mathbf{S}$ and $\mathbf{R}$, exhibits a very large number of local minima. This is illustrated in Fig. 1.

To assess the performance of TRUST, we considered a problem involving $N_s = 77$ shots and $N_r = 77$ receivers. A data set consisting of $N_t = 1462$ synthetic seismic traces folded over $N_k = 133$ common midpoint gathers was obtained from CogniSeis Corporation (20). The data set uses $N_f = 49$ Fourier components for data representation. Even though this set is somewhat smaller than typical collections obtained during seismic surveys by the oil industry, it is representative of the extreme complexity underlying residual statics problems. To derive a quantitative estimate of TRUST's performance, let E_k denote the total contribution to the stack power arising from midpoint k, and let B_k refer to the upper bound of E_k in terms of $\mathbf{S}$ and $\mathbf{R}$. Using a polar coordinates representation for the trace data D_{ft}, that is, $D_{ft} = \alpha_{ft} \exp(iw_{ft})$, we can prove (21) that

$$B_k = \sum_f \left(\sum_t \alpha_{ft} \delta_{kk_t} \right)^2 \quad (8)$$

The TRUST results, illustrated in Fig. 2, show the significant improvement in the coherence factor of each common gather. This factor is the ratio E_k/B_k and characterizes the overall quality of the seismic image.

In conclusion, the TRUST methodology for solving unconstrained global function optimization problems proves to be a powerful tool not only for academic problems; it has the robustness and consistency required by large-scale, real-life applications.

REFERENCES AND NOTES

1. H. Ratschek and J. Rokne, *New Computer Methods for Global Optimization* (Ellis Horwood, Chichester, UK, 1988).
2. A. Törn and A. Zilinskas, *Global Optimization* (Spring-
er-Verlag, Berlin, 1989).
3. R. Horst and H. Tuy, *Global Optimization* (Springer-Verlag, Berlin, ed. 2, 1993).
4. R. Horst and P. M. Pardalos, *Handbook of Global Optimization* (Kluwer, Dordrecht, Netherlands, 1995).
5. _____, N. V. Thoai, *Introduction to Global Optimization* (Kluwer, Dordrecht, Netherlands, 1996).
6. C. A. Floudas and P. M. Pardalos, *State of the Art in Global Optimization: Computational Methods and Applications* (Kluwer, Dordrecht, Netherlands, 1996).
7. H. Ammar and Y. Cherruault, *Math. Comput. Modeling* **18**, 17 (1993).
8. B. Cetin, J. Barhen, J. Burdick, *J. Optimization Theory Appl.* **77**, 97 (1993).
9. G. L. Bilbro, *IEEE Trans. Syst. Man. Cyber.* **24** (no. 4), 684 (1994).
10. I. P. Androulakis, C. D. Maranas, C. A. Floudas, *J. Global Optimization* **7**, 337 (1995).
11. M. Sen and P. L. Stoffa, *Global Optimization Methods in Geophysical Inversion* (Elsevier, Amsterdam, 1995).
12. D. Cvijovic and J. Klinowski, *Science* **267**, 664 (1995).
13. J. Barhen and V. Protopopescu, in *State of the Art in Global Optimization*, C. A. Floudas and P. M. Pardalos, Eds. (Kluwer, Dordrecht, Netherlands, 1996), pp. 163–180.
14. C. S. Adjiman and C. A. Floudas, *Global Optimization* **9**, 23 (1996).
15. P. M. Pardalos, D. Shalloway, G. Xue, Eds., *Global Minimization of Nonconvex Energy Functions: Molecular Conformation and Protein Folding*, vol. 23 of *Series in Discrete Mathematics and Theoretical Computer Science* (DIMACS) (American Mathematical Society, Providence, RI, 1996).
16. J. Barhen, M. Zak, N. Toomarian, in *Advanced Neu-*
ral Computers, R. Eckmiller, Ed. (North-Holland, Amsterdam, 1990), pp. 102–112.
17. D. Rothman, *Geophysics* **50**, 2784 (1985).
18. O. Yilmaz, *Seismic Data Processing* (Society of Exploration Geophysicists, Tulsa, OK, 1988).
19. J. DuBose, *Geophysics* **58**, 399 (1993).
20. The benchmark problem was provided by J. DuBose.
21. J. Barhen, D. Reister, J. DuBose, in preparation.
22. F. Aluffi-Pentini, V. Parisi, F. Zirilli, *J. Optimization Theory Appl.* **47**, 1 (1985).
23. L. Yong, K. Lishan, D. J. Evans, *Parallel Comput.* **21**, 389 (1995).
24. G. Schneider, J. Schuchhardt, P. Wrede, *Biol. Cybern.* **74**, 203 (1996).
25. A. H. G. R. Kan and G. T. Timmer, in *Numerical Optimization*, P. T. Boggs, R. H. Byrd, R. B. Schnabel, Eds. [Society for Industrial and Applied Mathematics (SIAM), Philadelphia, PA, 1985], pp. 245–262.
26. A. Levy and A. Montalvo, *SIAM J. Sci. Stat. Comput.* **6**, 15 (1985).
27. H. Szu and R. Hartley, *Phys. Lett.* **A122**, 157 (1987).
28. M. A. Styblinski and T. S. Tang, *Neural Networks* **3**, 467 (1990).
29. This research was performed at the Center for Engineering Systems Advanced Research, Oak Ridge National Laboratory. Funding provided by the Engineering Research Program of the Office of Basic Energy Sciences, and by the Advanced Computing Technology Initiative Program of the U.S. Department of Energy, under contract DE-AC05-96OR22464 with Lockheed Martin Energy Research Corporation. We thank Y. Y. Azmy, R. C. Mann, and T. H. Rowan for their comments and three unknown referees for their critical suggestions.

A Saturated X-ray Laser Beam at 7 Nanometers

J. Zhang,* A. G. MacPhee, J. Lin, E. Wolfrum, R. Smith, C. Danson, M. H. Key, C. L. S. Lewis, D. Neely, J. Nilsen, G. J. Pert, G. J. Tallents, J. S. Wark

A saturated nickel-like samarium x-ray laser beam at 7 nanometers has been demonstrated with an output energy of 0.3 millijoule in 50-picosecond pulses, demonstrating that saturated operation of a laser at wavelengths shorter than 10 nanometers can be achieved. The narrow divergence, short wavelength, short pulse duration, high efficiency, and high brightness of this samarium laser make it an ideal candidate for many x-ray laser applications.

An important objective in the development of x-ray lasers is to deliver a coherent, saturated output at wavelengths shorter

J. Zhang, E. Wolfrum, J. S. Wark, Clarendon Laboratory, Department of Physics, University of Oxford, Oxford, OX1 3PU, UK.
A. G. MacPhee and C. L. S. Lewis, School of Mathematics and Physics, Queen's University, Belfast, BT7 1NN, UK.
J. Lin, R. Smith, G. J. Tallents, Department of Physics, University of Essex, Colchester, CO4 3SQ, UK.
C. Danson and D. Neely, Central Laser Facility, Rutherford Appleton Laboratory, Chilton, Oxon, OX11 0QX, UK.
M. H. Key and J. Nilsen, Lawrence Livermore National Laboratory, Livermore, CA 94550, USA.
G. J. Pert, Department of Physics, University of York, York, YO1 5DD, UK.

*To whom correspondence should be addressed at Rutherford Appleton Laboratory, Chilton, OX11 0QX, UK. E-mail: j.zhang@rl.ac.uk

than 10 nm (1). Such saturated x-ray lasers are required for holography (2) and microscopy (3) of biological specimens and for deflectometry (4), interferometry (5), and radiography (6) of dense plasmas relevant to inertial confinement fusion and laboratory astrophysics (5). Saturated operation is important because it means that the maximum power possible for a given volume of excited plasma is extracted by the stimulated emission. Saturated x-ray lasers ensure an output energy sufficient for most applications and tend to produce a consistent output with little variation from shot to shot. Lasers are characterized by the product of the laser gain coefficient and the length of the laser region (gain-length product), and saturation requires a gain-

length product exceeding 15, which means millions-fold amplification by the stimulated emission.

The development of x-ray lasers has been marked by a progression toward successively shorter wavelengths. Saturation has been observed at wavelengths $\lambda > 15$ nm in neon-like x-ray lasers (lasers from ions with the electron configuration of neutral neon atoms) on the $J = 2 \rightarrow 1$ transitions in plasmas of germanium (7), selenium (8), and yttrium (9) and on the $J = 0 \rightarrow 1$ transition in zinc (10) and germanium (11) plasmas when driven by the largest optical laser facilities in the world. However, these x-ray lasers are difficult to scale to the shorter wavelengths ($\lambda < 10$ nm) required for most applications with the use of currently available laser driver energy because the driver energy required to produce the gain-length product approaching saturation increases rapidly in neon-like x-ray lasers for shorter wavelength operation. Nickel-like x-ray lasers, in principle, have a more favorable scaling of laser wavelength with drive-laser energy but have difficulties in providing a saturated output. Much effort has been devoted toward developing Ni-like x-ray lasers (12–14), but the resulting gain-length products and efficiency have been low. Recent experiments have shown that the intensity and efficiency of Ni-like x-ray lasers can be greatly enhanced by use of multiple equal-intensity short pulses at 400-ps intervals (15–18). A gain-length product of ~8 has been reported (15, 17); however, this value is still too low for saturated operation.

In the multipulse mode (19), the first pulse heats and ionizes the plasma, but the density gradients are too steep for laser propagation. The plasma expands, creating a plasma with a larger scale length and a larger, more uniform gain region that allows for good laser propagation (19–21). Aiming at improving efficiency and enhancing the gain-length product, we drove a Ni-like x-ray laser with a pulse configuration different from those used in experiments by other groups (15–18). Because it is not necessary to have a preplasma in an ionization stage as high as that needed for Ni-like materials, a low-intensity (~10 to 30% of the total energy) laser pulse (prepulse) was used to create a preplasma with a lower ionization configuration. The preplasma was then allowed to cool for a much longer time (>2 ns), until it became less transparent to the following laser pulse (main pulse), so that the plasma region, where laser gain generates, could directly absorb more energy from the main laser pulse before it hit the critical-density surface of the plasma. The long delay also provided an excited plasma column with a reduced density gradient, enabling the x-ray laser beam to propagate a longer distance at higher density and therefore to obtain sufficient amplification for saturation (11, 22). Here we describe a saturated x-ray laser beam at $\lambda < 10$ nm, specifically, the Ni-like Sm x-ray laser at 7 nm from a refraction compensating double target illuminated by a low-intensity prepulse 2.2 ns before the main drive-laser pulse.

The experimental setup is similar to that described in (11, 22) (Fig. 1). Three beams of the VULCAN Nd:glass laser at 1.05 μm with a 75-ps duration were used in a standard off-axis focus geometry, which provide a line focus with a 25-mm length and a 100-μm width, giving an irradiance of ~4.0×10^{13} W cm^{-2}. Deploying the other three beams in 180° opposition in a second line focus produced a plasma with an opposed density gradient, which helps compensate for the refraction of the x-ray laser beam from the first plasma (7, 11, 20, 22).

The flat slab targets, measuring 18 mm long, comprised 100-μm-wide Sm stripes coated on glass substrates. Both ends of the slab target were placed well within the line focus to avoid cold plasmas at the ends of the targets. The targets were aligned so that they were parallel with an adjustable separation (in the direction perpendicular to the target surfaces) between the surface planes and an axial separation of 500 μm between the two targets. Because the duration of the x-ray laser pulse is comparable to the propagation time, it is desirable to achieve a traveling wave excitation for the two successive targets to maximize the amplification. To approximate this condition, we timed the three drive beams for the first slab target to arrive 60 ps earlier than the three beams for the second target. The primary diagnostics along the target axis were two flat-field grazing incidence x-ray spectrometers with aperiodically ruled gratings of 1200 lines per millimeter (11, 22). They recorded the spectral range from 5.0 to 30.0 nm on InstaSpec IV x-ray charge-coupled-device (CCD) detectors (Oriel, Stratford, Connecticut). Radiation at wavelengths shorter than 6.0 nm was eliminated by use of two parallel silver mirrors at a 10° grazing incidence angle. Boron and parylene (CH) plastic filters provided variable attenuation up to 10^3 and absorption edges for wavelength calibration. The axial spectra in a given axial direction were recorded in either of two ways. Time-averaged spectra with angular resolution were obtained from an x-ray CCD detector in the focal plane. Alternatively, the Sm laser line at 7.3 nm was focused by the grating of the flat-field axial spectrometer into an x-ray streak camera so that the streak displayed the temporal variation of the angular distribution of the Sm laser line (22). The laser line width was less than 50 μm at the streak entrance plane, so the temporal resolution was lim-

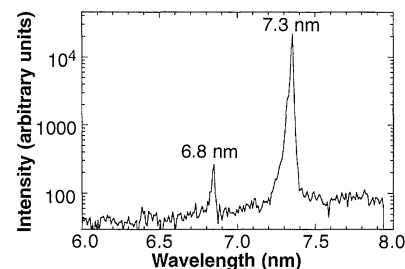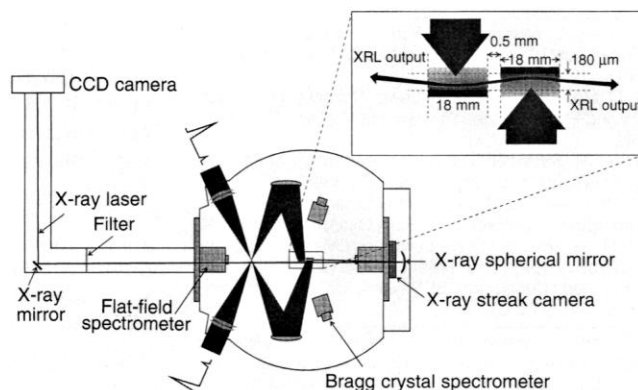**Fig. 2.** The time-integrated axial output spectrum from two coupled 18-mm-long, flat Sm targets separated by 175 μm. The laser line at 7.3 nm completely dominates the spectrum. The other laser line at 6.8 nm is also visible.

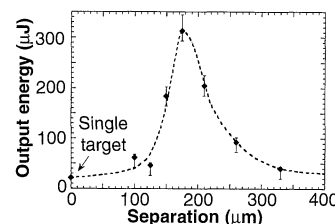**Fig. 3.** Output energy of the Sm x-ray laser at 7.3 nm versus the perpendicular separation between two opposing 18-mm-long plasmas.

Fig. 1. Schematic experimental setup.

ited to ~10 ps by the streak camera operation. A CCD detector recorded the time-resolved angular distribution. To measure the output energy, we cross-calibrated the on-axis spectrometers with a near field imaging system consisting of calibrated multilayer mirrors and an x-ray CCD detector (22–24), using the Ge laser at 19.6 nm (11) and the Ag laser at 14.0 nm (22) as the laser sources. This calibration assumes that the collection solid angle (50 mrad by 50 mrad) of the multilayer mirror system overfills the angular distribution of the x-ray lasers. The response of the CCD detector and the transmission of filters were calibrated with the use of x-ray radiation from a laser-produced plasma source coupled to a grating spectrometer (11, 25). Ionization balance and uniformity along the axial direction of both plasmas were monitored by space-resolving crystal spectrometers observing the resonance line emission of Ni-like and Co-like ionization stages in the ~6 to 12 Å region.

The on-axis output is completely dominated by the Ni-like Sm $4d \rightarrow 4p, J = 0 \rightarrow 1$ laser transition at 7.3 nm (Fig. 2). The other weak $4d \rightarrow 4p, J = 0 \rightarrow 1$ laser line at 6.8 nm is also visible (26). The intensity of the $J = 0 \rightarrow 1$ laser line at shorter wavelength will take over that at longer wavelength for elements of higher atomic number (12, 15). The intensity of the laser lines was attenuated by a factor of 50 with a combination of boron and CH filters to avoid saturation of the CCD detector.

The coupling of the double targets is optimized at a perpendicular separation near 175 μm (Fig. 3). Using the calibrated flat-field spectrometers, we can estimate the output energy of the Sm laser by integrating the total photons emitted from the x-ray laser. The maximum output energy of the Sm laser was 313 μJ, corresponding to a conversion efficiency 2×10^{-6}. The estimated uncertainty in this measurement is

within a factor of 3 and is due predominantly to uncertainty in the filter attenuation.

The output intensity of the Sm laser varied with target length (Fig. 4). The maximum length of a single target used in the experiment was 20 mm. The coupling efficiency at the optimized separation was quite high because of small deflection and divergence angles. For target plasmas with lengths <18 mm, the increase in output intensity of the laser line is a simple exponential form. The gain coefficient was determined by fitting the Linford formula to those data in the exponential region to be 8.4 ± 0.6 cm^{-1}. The output intensity no longer increases exponentially with target length for targets longer than 18 mm, which corresponds to a gain length product ~16, beyond which the output intensity only increases linearly and varies very little from shot to shot.

The peak emission from the double 18-mm target is about 10 times stronger than the emission from a single 18-mm-long flat target in x-ray streak images (Fig. 5). The laser emission from the single target has a broad divergence of 1.8 mrad and peaks 2.5 mrad off-axis. These small divergence and deflection angles provide some evidence of the improved density gradient resulting from the drive-pulse configuration. This setup also resulted in the efficient coupling between the two targets. The laser emission lasts about 37 ps, making this device one of
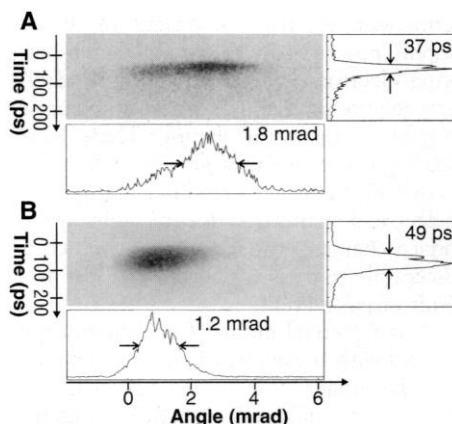
Fig. 5. Typical x-ray streak images of angular distributions of the Sm laser line at 7.3 nm from (**A**) a single target and (**B**) a double flat target with a perpendicular separation of 175 μm. At the right hand side are the temporal traces. At the bottom are the angular traces. The pulse durations are single scans through the angular peaks of the laser emission; the angularly integrated durations are about 10% longer. Similarly, the angular scans are single traces through the temporal peaks of the laser emission; the temporal integrated angular divergence is not very different from that measured by single traces. The gray levels of the two graphs were normalized to the same level to show the distributions for the different geometries.

the shortest pulse x-ray lasers yet produced. By comparison, the laser emission from a coupled double target shows strong coupling effects both angularly and temporally. Its pulse duration is somewhat longer (49 ps) because of the contribution from two targets, and its divergence is only 1.2 mrad, implying a spatial coherence length of ~5 μm at the exit plane of the x-ray laser. The beam from the double target is almost parallel to the target surface with a deflection angle as small as about 1 mrad. This small angle is certainly an advantage for applications. The angular distribution of the Sm laser in the direction parallel to the target surface also spreads over about 3.5 mrad. The angle of the peak intensity and divergence are influenced by refraction of the beam in the plasma. Both the deflection and divergence angles of the Sm laser (Fig. 5B) from a double target were compensated by the refraction-compensating double-target geometry.

Given our estimate of the upper limit of the source size (50 μm by 60 μm) from the knowledge of similar x-ray lasers (11, 22), the output intensity of the Sm laser was determined to be 2×10^{11} W cm^{-2}. The estimated uncertainty in this measurement is less than a factor of 2. It is of interest to compare the output intensity with the saturated intensity calculated for typical plasma conditions using XRASER kinetic simulations (27). The spontaneous emission rate of the upper laser level to the lower is calculated to be 0.35 ps^{-1}. Most of the upper level destruction rate is due to collisional mixing. The total destruction rate of the lower laser level is 4.5 ps^{-1}. In the simulations, typical plasma conditions for the Sm laser at 7.3 nm were used: an electron temperature of 700 eV and an electron density of 1×10^{21} cm^{-3}. The saturated intensity is then calculated to be 1.3×10^{11} W cm^{-2}, which agrees with the measured output. Taking into account the beam divergence (1.2 mrad by 3.5 mrad), a brightness of 2×10^{25} photons s^{-1} mm^{-2} mrad^{-2} is determined for the Sm laser at 7.3 nm.

In conclusion, we have demonstrated saturated operation of an x-ray laser at $\lambda <$ 10 nm using only about 4.0×10^{13} W cm^{-2} of intensity on target, that is, a focused intensity that can be achieved by smaller scale laser facilities. With the full ability of the VULCAN laser, saturated x-ray lasers at even shorter wavelengths near the water window should be possible.
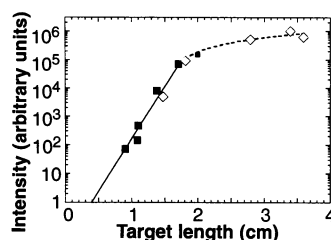

Fig. 4. Peak intensities as a function of target length. The solid line shows exponential increase of the output intensity and the broken line shows the linear increase of the output intensity in the saturation region. Solid squares are from single target data, and open diamonds from coupled target shots. Saturation intensity is reached at an approximate gain-length product of 16. The gain coefficient = 8.4 cm^{-1}.

REFERENCES AND NOTES

1. R. C. Elton, *X-Ray Lasers* (Academic Press, New York, 1990).
2. J. E. Trebes *et al.*, *Science* **238**, 517 (1987).
3. L. B. Da Silva *et al.*, *ibid.* **258**, 269 (1992).
4. D. Ress *et al.*, *ibid.* **265**, 514 (1994).

5. R. Cauble et al., ibid. **273**, 1093 (1996).
6. D. H. Kalantar et al., Phys. Rev. Lett. **76**, 3574 (1996).
7. A. Carillon et al., ibid. **68**, 2917 (1992).
8. J. A. Koch et al., ibid., p. 3291.
9. L. B. Da Silva et al., Opt. Lett. **18**, 1174 (1993).
10. P. Jaegle et al., in X-ray Lasers 1994 (AIP Conf. Proc. 332, American Institute of Physics, New York, 1994), pp. 25–34.
11. J. Zhang et al., Phys. Rev. A **54**, R4653 (1996).
12. B. J. MacGowan et al., Phys. Fluids B **4**, 2326 (1992).
13. C. L. S. Lewis et al., X-Ray Lasers 1992, E. E. Fill, Ed. (Conf. Ser. 125, Institute of Physics, 1992), pp. 23–30.
14. S. Basu et al., Appl. Phys. B **57**, 303 (1993).
15. H. Daido et al., Phys. Rev. Lett. **75**, 1074 (1995).
16. J. Nilsen and J. C. Moreno, Opt. Lett. **20**, 1387 (1995).
17. H. Daido et al., ibid. **21**, 958 (1996).
18. Y. Li et al., Phys. Rev. A **53**, R652 (1996).
19. C. H. Nam et al., Appl. Phys. B **50**, 275 (1990).
20. J. Nilsen and J. C. Moreno, Phys. Rev. Lett. **74**, 337 (1995).
21. J. Zhang et al., Phys. Rev. A **53**, 3640 (1996).
22. J. Zhang et al., in preparation.
23. G. Cairns et al., Appl. Phys. B **58**, 51 (1994).
24. J. Zhang et al., Phys. Rev. Lett. **74**, 1335 (1995).
25. I. Weaver, thesis, Queen's University, Belfast (1996).
26. J. H. Scofield and B. J. MacGowan, Phys. Scr. **46**, 361 (1992).
27. J. Nilsen, in Radiative-Hydro Modeling and Atomic Data Bases, A. Hauer and A. L. Merts, Eds. (AIP Conf. Proc. 168, American Institute of Physics, New York, 1988), pp. 51–58.
28. This work is part of a program on x-ray laser research funded by the Engineering and Physical Science Research Council under grants GR/L 11540, 11946, 11779, and 11809. E.W. has been supported by the Austrian Fonds zur Förderung der Wissenschaftlichen Forschung under project number P10844 NAW. The work of the authors at Lawrence Livermore National Laboratory (LLNL) was performed under the auspices of the U.S. Department of Energy by LLNL under contract W-7405-Eng-48.

Local, Nonvolatile Electronic Writing of Epitaxial Pb(Zr$_{0.52}$Ti$_{0.48}$)O$_3$/SrRuO$_3$ Heterostructures

C. H. Ahn, T. Tybell, L. Antognazza, K. Char, R. H. Hammond, M. R. Beasley, Ø. Fischer, J.-M. Triscone

A scanning probe microscope was used to induce local, nonvolatile field effects in epitaxial, ferroelectric Pb(Zr$_{0.52}$Ti$_{0.48}$)O$_3$/SrRuO$_3$ heterostructures. Field-effected regions with linewidths as small as 3500 angstroms were written by locally switching the polarization field of the Pb(Zr$_{0.52}$Ti$_{0.48}$)O$_3$ layer; the electronic density of the underlying metallic SrRuO$_3$ layer was modified and the sheet resistance was changed by up to 300 ohms per square. This procedure is completely reversible and allows submicrometer electronic features to be written directly in two dimensions, with no external electrical contacts or lithographic steps required.

Ferroelectric materials are characterized by a nonvolatile, reversible polarization field that has been successfully used in applications such as radiation hard memories (1). With advances in thin-film oxide growth, epitaxial conducting oxide–ferroelectric and high-temperature superconductor–ferroelectric heterostructures have recently been fabricated, and ferroelectric switching with improved fatigue properties has been observed, as have ferroelectric field effects in materials with relatively large carrier densities (2–4). Progress has also been made in the switching and imaging of the surface charge distribution and topographic deformations of small ferroelectric domains in bulk crystals and polycrystalline films using scanning force and optical probes (5–8).

Here, we investigated another opportunity afforded by the nonvolatile polarization of epitaxial ferroelectric oxides with high surface quality. We have devised a technique that produces a nonvolatile, local doping in a thin film using conducting oxide–ferroelectric heterostructures. This approach allows direct and reversible writing of submicrometer electronic structures by means of scanning probe microscopy; no permanent electrical contacts or lithographic processes are required, whereas existing electronic devices that use field effects require such contacts and lithography to achieve electronic doping. These local electronic nanofeatures also provide a detection mechanism to read out written ferroelectric domains that does not rely on the surface charge of the ferroelectric, which is susceptible to deterioration of contrast as a result of passivation.

A commercial atomic force microscope (AFM) with a metallized tip was scanned over the surface of an epitaxial ferroelectric Pb(Zr$_{0.52}$Ti$_{0.48}$)O$_3$ (PZT)/SrRuO$_3$ heterostructure (Fig. 1) while a voltage was applied between the tip and the ultrathin metallic SrRuO$_3$ film. When the coercive field of the PZT layer was exceeded, the ferroelectric polarization switched directly underneath the tip and induced screening charges to flow in the SrRuO$_3$ layer, changing the total carrier concentration and hence the conductivity of the material.

We used epitaxial PZT/SrRuO$_3$ heterostructures that are well suited for application of a ferroelectric field effect and that can be grown with high quality and low roughness over large areas, which is impor-

tant for these scanning experiments (4). For the growth of SrRuO$_3$, we carried out reactive molecular-beam epitaxy (MBE) in an ultrahigh-vacuum electron-beam evaporation system (4, 9). X-ray diffraction patterns on thick (1000 to 5000 Å) samples revealed epitaxial growth of SrRuO$_3$(110) on SrTiO$_3$(001) substrates, with SrRuO$_3$ [001] parallel to SrTiO$_3$ [100]. The rocking curve taken around the 220 reflection has a full width at half maximum (FWHM) of 0.03°. Transport measurements taken on these films revealed large residual resistivity ratios (as high as 33). Ultrathin films were required for substantial field effects to be observed. Epitaxial metallic films (30 Å thick) were grown and characterized with in situ ultraviolet photoelectron spectroscopy (UPS), reflection high-energy electron diffraction (RHEED), and low-energy electron diffraction (LEED) measurements, followed by ex situ transport measurements. AFM images taken on these films revealed a root-mean-square surface roughness of 1.5 Å over a 6 μm by 6 μm area.

Afterward, tetragonal PZT was deposited onto the SrRuO$_3$ by means of off-axis radio frequency sputtering (10). X-ray diffraction revealed (001) growth on SrRuO$_3$, with PZT [100] parallel to SrRuO$_3$ [001]. The rocking curve of the PZT 001 reflection has a FWHM of 0.09°. For these films, the two ferroelectric polarization states lie perpen-
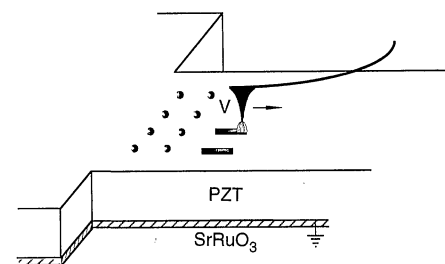

Fig. 1. Schematic of the PZT/SrRuO$_3$ heterostructure. With the use of an AFM with a metallized tip, ferroelectric domains can be polarized by applying a voltage between the tip and SrRuO$_3$ film that exceeds the coercive field of the PZT layer, resulting in a local, nonvolatile change in the electronic properties of the underlying film.

C. H. Ahn, T. Tybell, L. Antognazza, Ø. Fischer, J.-M. Triscone, Département de Physique de la Matière Condensée, University of Geneva, 24 Quai Ernest-Ansermet, 1211 Geneva 4, Switzerland.
K. Char, Conductus Inc., 969 West Maude Avenue, Sunnyvale, CA 94086, USA.
R. H. Hammond and M. R. Beasley, Department of Applied Physics, Stanford University, Stanford, CA 94305, USA.